Enhancement photoresponse in facile Zn-doped β-Ga_2O_3 photodetectors

Naresh Sharma[*] and Satinder K. Sharma[†]
School of Computing and Electrical Engineering, Indian Institute of Technology (IIT) Mandi, Mandi 175005, Himachal Pradesh, India

(Received 5 April 2026; accepted 6 October 2026; published 9 November 2026)

In this work, we report a sol-gel-based combustion process for the formulation of gallium oxide (β-Ga_2O_3) to develop robust UV-C (200–280 nm) photodetectors. Controlled Zn incorporation is employed to modulate the optical and electronic properties of β-Ga_2O_3. The devices are fabricated on a *c*-plane sapphire (0001) substrate, and a comparative analysis is performed for varying Zn dopant concentrations. Planar metal-semiconductor-metal structures with 50-μm-wide interdigitated aluminum electrode architecture are realized using standard photolithographic and processing techniques. The optimized photodetector devices exhibit a high responsivity, low rise time, and high photocurrent/dark current ratio of ∼20 mA/W, ∼2 s, and $\sim 10^4$ in the UV-C range, associated with Zn-dependent modification of the material's optical response, local electronic environment, and carrier transport/trapping processes. It establishes the Zn-doped β-Ga_2O_3 as a promising platform for robust, low-cost, and high-performance solar-blind UV-C photodetector applications.

DOI: 10.1103/3ft2-4nhl

I. INTRODUCTION

Solar radiation entering the Earth's atmosphere spans a wide range of wavelengths (λ) with varying effects on human health and the environment. Among these, ultraviolet (UV) radiation particularly has an adverse, harmful effect, leading to skin cancer and other health issues. The UV spectrum is broadly divided into UV-C (200–280 nm), UV-B (280–315 nm), and UV-A (315–400 nm) [1]. Whereas the ozone layer present between the troposphere and the stratosphere absorbs UV-C and most UV-B, particularly UV-C is strongly absorbed by the Earth's atmosphere. Consequently, UV-C is highly suitable for detector applications, as it enables solar-blind operation with negligible background radiation at the ground level. In this context, UV photodetectors typically offer low noise and high sensitivity, making them attractive for various applications. Particularly, UV photodetectors have broad utility in defense for missile plume detection, early warning systems, stealth tracking, and surveillance because UV emissions from high-temperature rocket exhausts can be detected without background noise, which is critical for rapid alert systems [1]. UV photodetectors are exclusively used in the medical field for chemical and biological assays, skin disease monitoring, sterilizing of medical equipment, and sensitive imaging of biomolecules [2]. Today, electronic gadgets are almost ubiquitous across fields, including healthcare, biomedical [3], automotive, and defense technologies [3,4]. In parallel, growing environmental concerns with

[*]Contact author: nareshsharma0809.ns@gmail.com
[†]Contact author: satinder@iitmandi.ac.in

Published by the American Physical Society under the terms of the Creative Commons Attribution 4.0 International license. Further distribution of this work must maintain attribution to the author(s) and the published article's title, journal citation, and DOI.

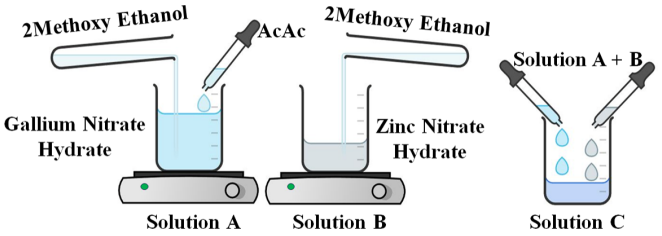


FIG. 1. Two different solutions with 1:1 mM of gallium nitrate hydrate:acetyl acetone and zinc nitrate hydrate in 2ME were made separately and then precisely mixed in different concentrations of Ga:Zn to form a homogeneous solution.

respect to global warming and ozone layer thinning have intensified the demand for UV photodetectors as a reliable monitoring system for detecting and issuing early warnings of harmful radiation [5] and UV damage assessment. There is an urgent demand for low-cost, scalable UV detectors that offer robust performance, high sensitivity, and fast response times. Given their broad range of applications, key performance metrics such as scalability, sensitivity, rapid response, and low-voltage operation are critical design considerations. Among wide-bandgap semiconductors, β-Ga_2O_3 has emerged as a promising candidate due to its ultrawide bandgap (4.5–5.3 eV), excellent chemical and thermal stability [6], and inherent solar-blind nature [7],[8]. Ga_2O_3 belongs to the family of transparent conducting oxides [9], which exists in six different polymorphs, namely, α-, β-, γ-, ε-, δ-, and κ-Ga_2O_3. Among all these, polymorph β-Ga_2O_3 is one of the most thermodynamically stable mesomorphs [10]. Furthermore, bandgap and defect engineering through controlled Zn doping offers a pathway to tailor the electronic structure of β-Ga_2O_3, enabling optimized carrier concentration, suppression of deep trap states, and enhanced photoresponsivity.

Conventional, thin-film growth techniques such as sputtering [11], pulsed laser deposition [12,13], molecular beam epitaxy [14], chemical vapor deposition [15], and metal organic chemical vapor deposition (MOCVD) [16] can produce high-quality β-Ga_2O_3 but are prohibitively expensive due to complex instrumentation, high machinery costs, stringent vacuum requirements, and sophisticated operations [17]. In contrast, solution-based methods, particularly sol-gel processing, offer a low-cost, scalable alternative, while maintaining detector accuracy and low-voltage operation. Several studies have demonstrated the viability of sol-gel-driving thin films using different precursors, environmental conditions, and various substrates. For example, Shen *et al.* reported a β-Ga_2O_3 thin film for UV photodetectors via sol-gel processing and achieved a fast response time after annealing at 700 °C [18], whereas Vronskii *et al.* used different substrates to deposit β-Ga_2O_3 thin films and found that sapphire substrates annealed at 1100 °C yield superior crystallinity compared to quartz and Si [19].

In this work, we present solution-processed β-Ga_2O_3-based UV-C photodetectors [20] fabricated on *c*-plane sapphire substrates with precisely controlled Zn doping, aiming to achieve low-cost fabrication, enhanced sensitivity, and fast photoresponse suitable for UV-C detection. A systematic comparative analysis is performed across varying Zn concentrations to identify optimal doping conditions for maximum performance, establishing a robust, scalable, and economically viable pathway for next-generation UV photodetectors.

II. METHODS

Gallium oxide, sol-gel precursor solutions were prepared by dissolving gallium nitrate hydrate (Sigma-Aldrich) and acetylacetone in a 1:1 mmol/ml in 4 ml of 2-methoxyethanol (2ME) christened as solution A. Similarly, a 2 ml zinc precursor solution was synthesized from zinc nitrate hydrate in 2-methoxyethanol under identical conditions and designated as solution B, shown in Fig. 1.

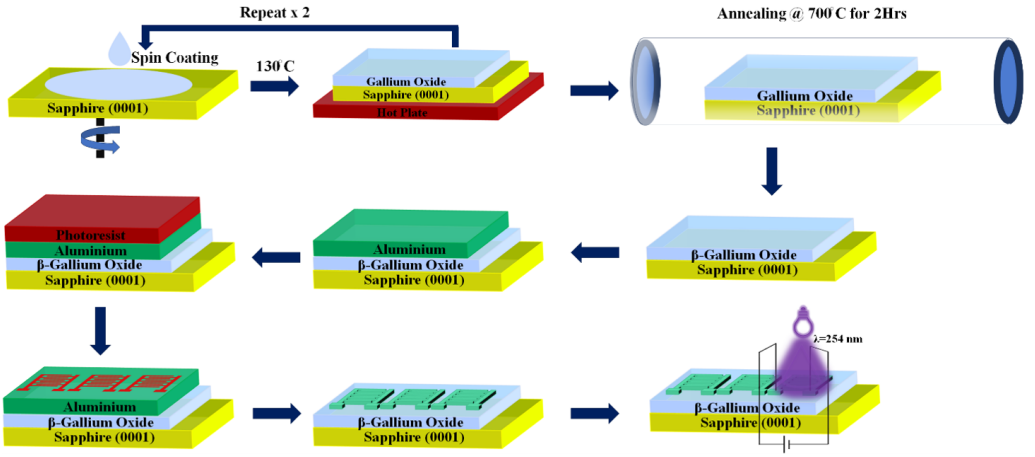


FIG. 2. Process flow for the fabrication of a UV photodetector device via the sol-gel process on a *c*-plane sapphire substrate.

Both solutions, A and B, were magnetically stirred at 80 °C for 8 h at 500 rpm and subsequently aged for 12 h at room temperature. To methodologically investigate the effect of Zn incorporation, Ga:Zn mixtures with varying volume ratios (0%, 0.5%, 1%, 3%, and 5%) were prepared for comparative analysis.

Single-side polished *c*-plane sapphire (0001) wafers were diced into 1×1 cm^2 samples and sequentially cleaned by ultrasonication in deionized water (10 min), acetone (15 min), and isopropanol (15 min), followed by nitrogen purging and soft baking at 90 °C for 10 min. To further enhance surface wettability and film adhesion, the substrates were treated with UV-ozone prior to film deposition [21].

Thin films were deposited by spin coating at 3000 rpm for 30 s, followed by soft baking at 130 °C for 15 min; two coating cycles were applied for each set of samples. The coated samples were annealed at 700 °C for 2 h in an argon atmosphere (50 sccm) using a three-zone furnace, with a controlled ramp rate and natural cooling, to induce the β-Ga_2O_3 phase [22]. Aluminum electrodes were deposited by thermal evaporation and subsequently patterned using standard photolithography. A positive photoresist (S1813) was spin coated at 5000 rpm for 1 min, soft baked at 110 °C for 1 min, exposed under UV light ($\lambda \sim 365$ nm) using an EVG-610 mask aligner, and developed in standard MF-319 developer, followed by deionized (DI) water rinsing. The Al layer was subsequently patterned by wet etching in an H_3PO_4:HNO_3:DI water (19:1:4) solution, yielding interdigitated electrode arrays with 50 μm linewidth and 50 μm (1:1) spacing. The exact process flow is shown schematically in Fig. 2 as well.

III. RESULTS

A. Material characterization

The structural properties of the Zn-doped Ga_2O_3 thin films were first examined using x-ray diffraction (XRD). The diffraction patterns [Fig. 3(a)] displayed well-defined peaks at 19.46°, 38.98°, and 59.66°, corresponding to the monoclinic β-Ga_2O_3 phase, respectively [23–25]. This indicates that the deposited samples are in the (−201) orientation, which is thermodynamically more favorable over the *c*-plane orientation on the sapphire substrate. A strong peak observed at 43° was attributed to the sapphire (0001) substrate [15], confirming that the sol-gel-derived films crystallized into the desired β phase upon annealing at 700 °C [19]. The absorption spectra and corresponding. Tauc-derived [Fig. 3(b), inset] apparent optical transition energies are approximately 4.48, 4.44,

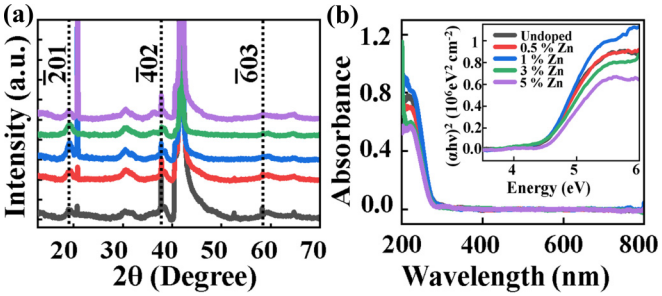


FIG. 3. (a) XRD plot for different concentrations of zinc. (b) Absorption spectrum and Tauc plot of the thin film with varying concentrations of Zn.

4.44, 4.42, and 4.61 eV for 0%, 0.5%, 1%, 3%, and 5% Zn, respectively. Thus, the extracted optical transition energy exhibits a modest and nonmonotonic dependence on Zn concentration. Since the Tauc construction does not explicitly account for excitonic interactions, Urbach-tail broadening, or Zn/defect-related localized states, these values are used primarily for comparative assessment of films processed under identical conditions rather than as direct measurements of the quasiparticle bandgap. Consequently, the observed variation should not be uniquely attributed to bandgap engineering.

Hence, the bandgap was calculated from the absorbance spectra and performing the linear fitting of the Tauc plot [26]. The reduction in the bandgap with increasing Zn concentration can be attributed to the formation of impurity-induced localized strain arising from structural rearrangements and defects, in line with other reports [27].

Figure 6 represents the x-ray photoelectron spectroscopy (XPS) spectra of the samples with varying concentration, increasing from bottom to top in the plots. In Fig. 6(b), we can see that the bottom curve of undoped β-Ga_2O_3 shows no Zn peak, whereas the doped samples exhibited two different peaks, one for Zn $2p^{3/2}$ and the other for Zn $2p^{1/2}$, verifying the successful incorporation of Zn into the Ga_2O_3 lattice with the plots shifting toward lower binding energy as the concentration increases. The high-resolution XPS spectra of O 1*s* (Fig. 4) and Ga 3*d* (Fig. 5) core levels are deconvoluted to investigate the influence of Zn incorporation on the chemical states of β-Ga_2O_3. The O 1*s* spectra were deconvoluted into two components in the range of 530.9–531.2 and 532.5–532.8 eV, corresponding to lattice oxygen (O^{2-}) and oxygen vacancy, respectively. Quantitative analysis of the peak areas confirmed that the dominant component was lattice oxygen (92.27%–93.45%), while the oxygen-vacancy-related component varied only slightly (6.55%–7.73%) for all samples. The Ga 3*d* spectra were fitted to Ga^+ (∼19 eV), Ga^{3+} (∼20.5 eV), and O 2*s* (∼23.2 eV) components. The Ga^{3+} contribution remained nearly constant (∼83.5%) with Zn incorporation, while only a small variation in the Ga^+ was observed, indicating that Zn is primarily incorporated without significantly altering the oxidation state of gallium. Furthermore, the lattice O 1*s* and Ga^{3+} peaks showed a gradual shift of ∼0.3 eV toward lower binding energy with increasing Zn concentration, indicating a slight modification of the local electronic environment due to Zn incorporation. The results indicate that Zn incorporation modifies the local chemical environment, but the β-Ga_2O_3 lattice remains largely intact, and the defect concentration remains relatively constant. The faster response observed for the 3% Zn-doped device may arise from an optimized balance among photocarrier generation, trapping, transport, and recombination.

Zn incorporation modifies the local electronic environment and may alter the energetic distribution or activity of defect/trap states without necessarily producing a large change in the total oxygen-vacancy-related XPS component. Since the present measurements do not directly resolve individual trap states or their densities, this mechanism is proposed as a plausible interpretation rather than definitive evidence [28–30].

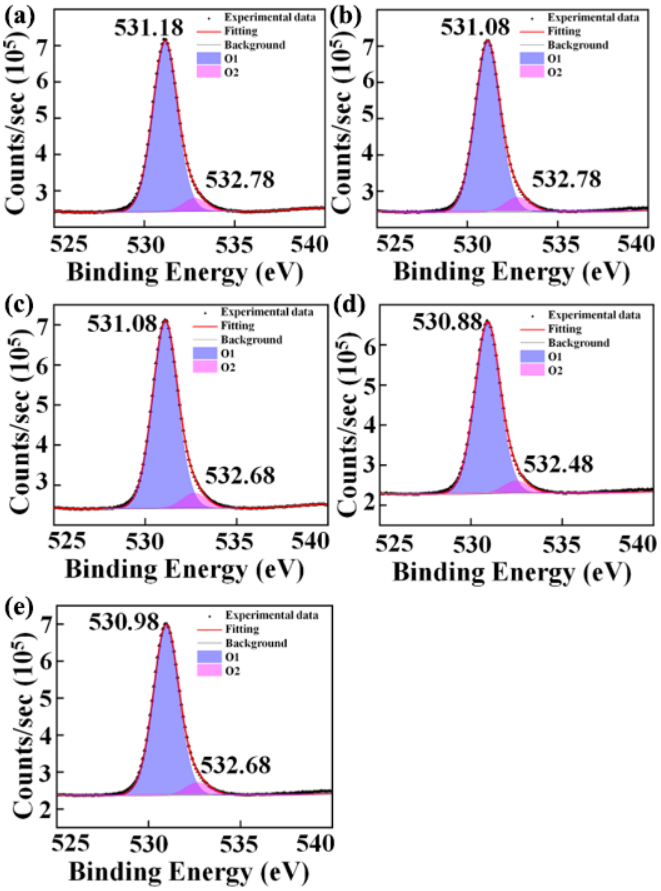


FIG. 4. Deconvoluted peaks of O 1*s* spectra. (a) Undoped β-Ga_2O_3, (b) 0.5% Zn doped, (c) 1% Zn doped, (d) 3% Zn doped, and (e) 5% Zn doped.

Figure 6(e) shows the characteristic Raman peaks at around 203 cm^{-1} (Ag^3), 416 cm^{-1} (Ag^6), and 751 cm^{-1} (Ag^{10}). The Ag^3 mode is derived from mixed Ga–O vibrations, while Ag^6 and Ag^{10} involve increasingly stronger oxygen-related vibrations in the Ga–O. Zn could have substituted on Ga lattice sites; it might have only disturbed the local Ga–O bonding environment without changing the β-Ga_2O_3 crystal symmetry. The characteristic Raman modes remain unchanged, and no extra peaks are observed, indicating that the monoclinic β-Ga_2O_3 phase is retained after Zn doping.

All three modes can be seen in the Raman spectra, with a low-frequency mode at $\sim$203 cm^{-1}, a medium-frequency mode at $\sim$416 cm^{-1}, and a high-frequency mode at $\sim$751 cm^{-1}, which are in good agreement with the previous experimental findings [23,31].

Figure 7(f) summarizes the variation in the rms surface roughness of the Zn-doped β-Ga_2O_3 thin films. The roughness initially decreases from 0.634 ± 0.01 nm for the undoped film to 0.563 ± 0.018 and 0.552 ± 0.015 nm for the 0.5% and 1% Zn-doped films, respectively, indicating that low Zn concentrations promote a smoother and more compact film surface. At higher Zn concentrations (3% and 5%), the rms roughness increases slightly to 0.653 ± 0.019 and 0.683 ± 0.012 nm, respectively. This increase is likely associated with dopant-induced lattice distortion and local structural disorder during film growth. The roughness remains below 1 nm for all samples, indicating that the deposited films have good surface uniformity. Although surface morphology can affect carrier scattering and interface quality, the observed variations in optoelectronic performance

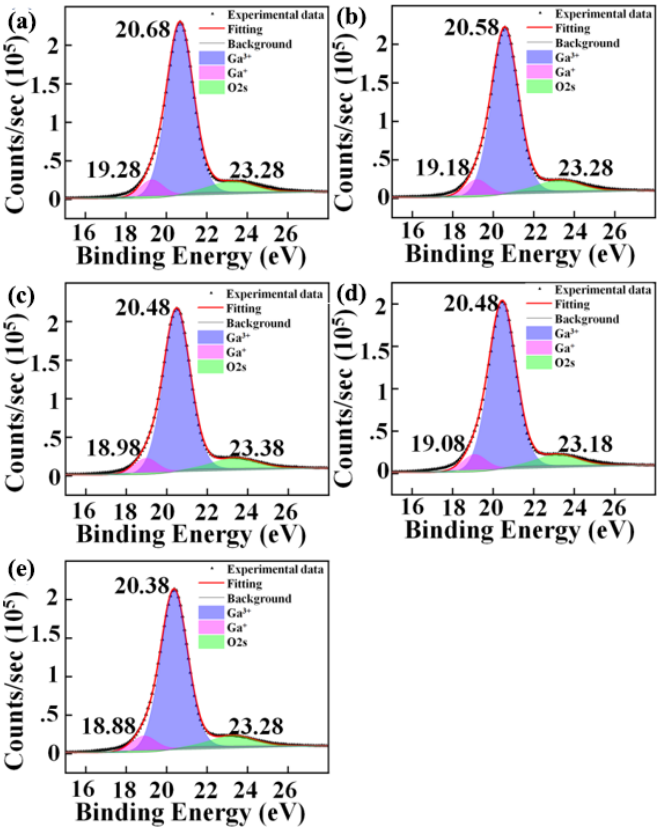


FIG. 5. Deconvoluted peaks of Ga 3*d* spectra. (a) Undoped β-Ga_2O_3, (b) 0.5% Zn doped, (c) 1% Zn doped, (d) 3% Zn doped, and (e) 5% Zn doped.

are considerably larger than the relatively small changes in roughness. Therefore, the electrical characteristics are primarily attributed to Zn-induced modifications in carrier concentration, defect states, and charge transport mechanisms rather than to surface morphology alone.

B. Electrical characterization

The responses of dark current and photocurrent at different bias voltages were measured by using a Keithley 4200, four-probe semiconductor characterization system. A source of UV light ($\lambda \sim 254$ nm) was illuminated on the samples; all photoresponse measurements were performed using the same light source with measured incident optical power density of 1.2 mW/cm^2 from a fixed height while performing the electrical characterization. The bright current (photocurrent) was measured; the dark current was measured after turning off the UV light source, under identical biasing conditions.

All the samples with different Zn concentrations (0%, 0.5%, 1%, 3%, and 5% v/v) were characterized at different bias voltages to evaluate transport behavior and bias dependence. Based on signal stability, signal-to-noise ratio, and reproducibility, a bias voltage of 2 V was selected for comparative performance analysis across all compositions. The resulting current density versus voltage characteristics plots are shown in Fig. 8. The shift in the origin of the dark current is due to the charge traps at the interface of the metal and semiconductor junction of metal-semiconductor-metal (MSM) structures [32,33]. These interfacial traps modify the effective Schottky barrier and contribute to variations in asymmetry and offset in the dark current characteristics of device structures. It is

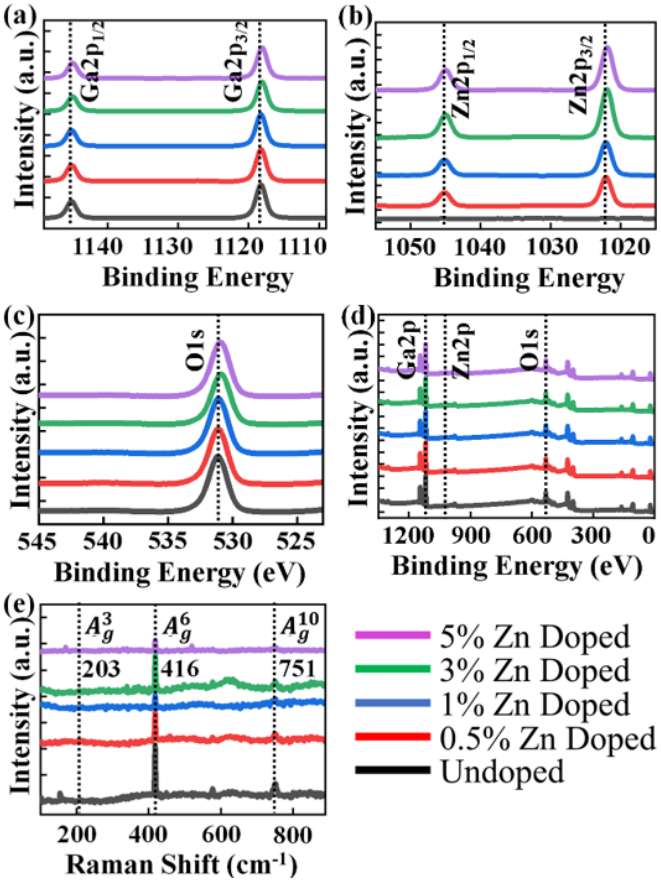


FIG. 6. XPS curve of β-Ga_2O_3 thin film: (a) gallium peaks, (b) Zn peaks, (c) oxygen peaks, (d) complete XPS plots, and (e) Raman spectra of all the samples.

attributed to excessive dopant-induced defect formation, increased trap density, and enhanced carrier recombination, which collectively suppress charge transport and photogeneration efficiency [34,35]. The *J*–*V* plots (Fig. 8) revealed that the 3% and 5% Zn-doped device structures exhibited the highest

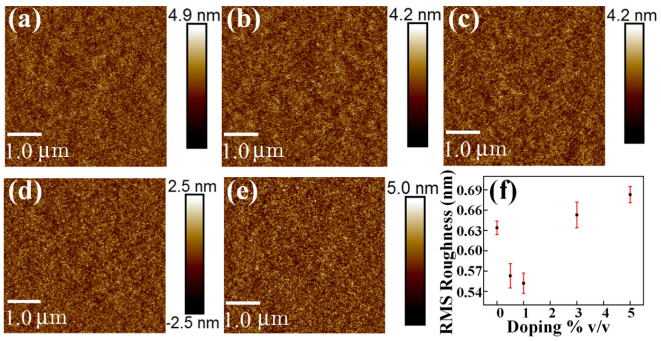


FIG. 7. AFM images of thin film. (a) Undoped β-Ga_2O_3, (b) 0.5% Zn doped, (c) 1% Zn doped, (d) 3% Zn doped, (e) 5% Zn doped, and (f) comparison plot for rms roughness with different doping concentrations.

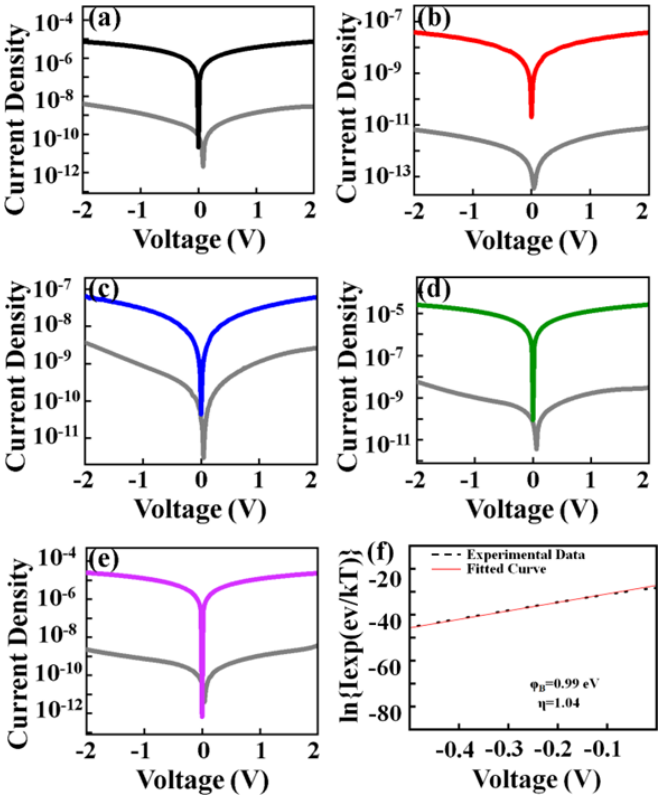


FIG. 8. Current density (A/cm^2) vs voltage curve for different concentrations of Zn-doped gallium oxide. (a) Undoped, (b) 0.5% Zn-doped, (c) 1% Zn-doped, (d) 3% Zn-doped, and (e) 5% Zn-doped β-Ga_2O_3, and (f) $\ln\{I\exp(eV/kT)\}$ vs V plot to calculate the Schottky barrier height.

photocurrent-to-dark current ratio, with nearly 10^3 and 10^4 orders of magnitude separation at 2 V bias. Metal-semiconductor-metal photodetectors (MSM-PDs) functionality hugely depends upon the Schottky barrier height. Therefore, controlling the Schottky barrier height and junction ideality factor is an important parameter in the device fabrication. Evaluation of Schottky barrier height is complicated due to two serially connected back-to-back Schottky junctions in an MSM structure [36]. The reversed biased junction of the MSM-PD plays a critical role in calculating the barrier height as the amount of current flowing through the device is governed by this junction. Averine *et al.* [37] proposed a current voltage relation for $V < 0.5$ and $T < 350$ K, which can be written as

$$I\exp\frac{eV}{kT} = I_o\exp\frac{eV}{\eta kT},$$

where I is the current, I_o is reverse saturation current, V is the applied voltage, η is the junction ideality factor, k is the Boltzmann constant, and T is the absolute temperature. I_o was calculated by fitting the $\ln\{I\exp\frac{eV}{kT}\}$ versus V plot and marking Y intercept at $V = 0$ shown in Fig. 8(f). The Schottky barrier height can be calculated from the following relation:

$$I_o = AA^*T^2\exp\frac{-e\Phi_B}{kT},$$

where A is the active device area, A^* is the Richardson constant, e is the charge on electron, and Φ_B is the Schottky barrier height.

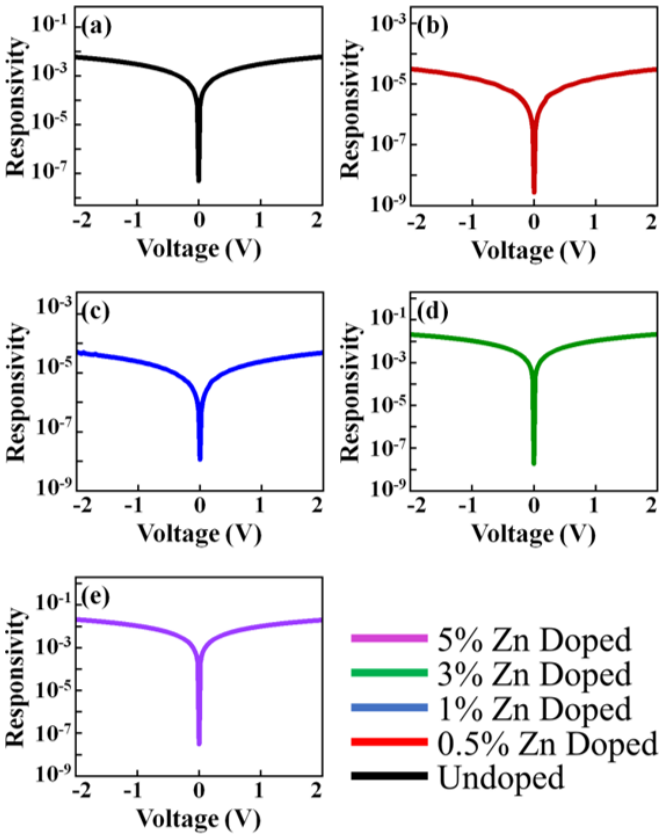


FIG. 9. Responsivity of the photodetector at 1.2 mW/cm^2 optical power with 2 V bias. (a) Undoped, (b) 0.5% Zn-doped, (c) 1% Zn-doped, (d) 3% Zn-doped, and (e) 5% Zn-doped β-Ga_2O_3.

The results show that the Schottky barrier height remains nearly constant, varying only within a small range of approximately 0.94–0.99 eV. The Schottky barrier heights are 0.94, 0.97, 0.95, 0.99, and 0.95 eV for undoped, 0.5%, 1%, 3%, and 5% Zn-doped samples. This indicates that Zn incorporation has only a minor effect on the metal/β-Ga_2O_3 Schottky barrier. The observed variations in the electrical and photoresponse characteristics with Zn doping are therefore more likely associated with changes in the material properties, such as carrier concentration, defect density, and trap states, rather than significant modifications of the metal-semiconductor barrier itself. The charge transfer depends on not only the barrier but other factors too, such as trap-assisted conduction that happens in lower bias voltage, while carrier tunneling and charge recombination happen at higher bias voltages.

The responsivity of the fabricated β-Ga_2O_3 photodetectors was calculated at a 2 V bias, as shown in Fig. 9. The values are 5.92 mA/W, 31.4 μA/W, 49.3 μA/W, 20.3 mA/W, and 20.9 mA/W for 0%, 0.5%, 1%, 3%, and 5% Zn doping, respectively. With an incident optical power of 1.2 mW/cm^2, the device with 3% and 5% Zn doping achieved a maximum responsivity of ∼20 mA/W. These results confirm that Zn incorporation at optimal concentrations enhances the optoelectronic response of β-Ga_2O_3 photodetectors. The responsivity is calculated as follows:

$$\text{Responsivity} = \frac{I_{\text{ph}} - I_{\text{dark}}}{P_{\text{opt}}},$$

where I_{ph} is the photocurrent under light, I_{dark} is the dark current, and P_{opt} is the optical power.

TABLE I. Performance comparison of various Zn-doped and undoped β-Ga_2O_3-based photodetectors.

Material	Fabrication technique	Bias	Responsivity	Detectivity	Photocurrent/dark current ratio
Undoped β-Ga_2O_3 [18]	Sol-gel spin coating	NR	NR	NR	18.34
α/β-Ga_2O_3 [41]	Sol-gel spin coating	15 V	NR	5.41×10^{11} Jones	1664
Undoped β-Ga_2O_3 [42]	Sol-gel spin coating	10 V	20 mA/W	NR	430.5
Sn:β-Ga_2O_3 [43]	Sol-gel spin coating	30 V	164 mA/W	3.21×10^{12} Jones	~6000
Zn:β-Ga_2O_3 (fixed concentration) [39]	MOCVD	20 V	210 A/W	NR	NR
Zn:β-Ga_2O_3 (fixed concentration) [44]	Spray pyrolysis	20 V	0.393 mA/W	2.65×10^{10} Jones	NR
This work	Sol-gel spin coating	2 V	20.9 mA/W	~10^{11} Jones	~10^4

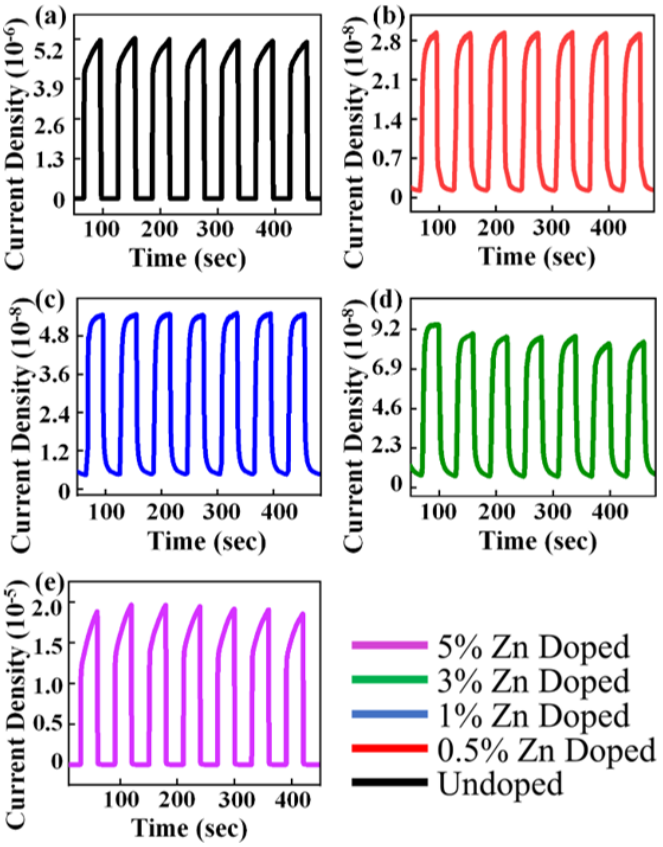


FIG. 10. Current density vs time curve for measuring the rise time of the photodetector. (a) 0% Zn-doped, (b) 0.5% Zn-doped, (c) 1% Zn-doped, (d) 3% Zn-doped, and (e) 5% Zn-doped gallium oxide UV detector.

The current density versus time characteristics were also measured to determine the dynamic photoresponse behavior and how quickly the photodetectors respond to UV light when irradiated on the sensor. The characteristics are plotted in Fig. 10 for both Zn-doped and undoped β-Ga_2O_3 devices. Here, the UV light source was kept on for 30 s, then off for 30 s, and so on. The rise range was kept from 10% to 90%; the calculated rise times are 8.93, 7.24, 5.85, 2.02, and 5.9 s for 0%, 0.5%, 1%, 3%, and 5% Zn doping, respectively. From the results obtained, it clearly indicates that with 3% Zn doping, the UV photodetector has a minimum rise time of around 2.02 s. The markedly faster response observed at 3% Zn doping can be attributed to an optimal balance between carrier generation and recombination, resulting from reduced deep-level trap density and improved carrier transport pathways [34]. The improved dynamics were attributed to Zn substitution, which effectively suppresses oxygen-vacancy-related deep trap states, thereby facilitating faster carrier release and recombination processes [38,39]. In contrast, the slower response observed in undoped and heavily doped devices suggests the presence of higher trap densities that prolong carrier lifetime and delay current stabilization [40].

The specific detectivity (D^*) was also evaluated for the fabricated β-Ga_2O_3 photodetectors to quantify their ability to detect weak optical signals in the presence of noise. Specific detectivity (D^*) was calculated using the following expression:

$$D^* = \frac{(\sqrt{A}) \times R}{\sqrt{2el_{\text{dark}}}},$$

where A is the device area, R is the responsivity, e is the electron charge, and I_{dark} is the dark current of a photodetector. The detectivity for different Zn-doped samples shown in Fig. 11 is in the order of 10^{10}, 10^8, 10^8, 10^{11}, and 10^{11} Jones for 0%, 0.5%, 1%, 3%, and 5% Zn doping, respectively. From here, it can be concluded that the 3% and 5% Zn-doped samples exhibit a maximum detectivity of 10^{11} Jones. Among the investigated compositions, the prototype β-Ga_2O_3 photodetectors with 3% and 5% Zn doping exhibited the highest detectivity ($\sim 10^{11}$ Jones), primarily due to their enhanced responsivity combined with suppressed dark current. This improvement highlights the beneficial role of Zn incorporation in modulating defect states and improving signal discrimination capability in β-Ga_2O_3 photodetectors. To evaluate the performance of the fabricated photodetectors, a comparative analysis of sol-gel and other solution-processed β-Ga_2O_3-based UV photodetectors is presented in Table I. The comparison considers key device parameters and reports photo response characteristics to highlight the performance of the present work relative to existing literature.

IV. CONCLUSION

The UV photodetectors fabricated using the solution-processed sol-gel route demonstrate competitive performance, particularly in terms of fast response speed and high detectivity, while employing a comparatively low annealing temperature of 700 °C to achieve the desired crystalline β-Ga_2O_3 phase. Precise control of Zn doping in the β-Ga_2O_3 precursor solution significantly alters the photodetector's response compared to the undoped device, enabling optimization of sensitivity, responsivity, and rise time. However, excessive Zn incorporation introduces additional recombination centers and trap states, ultimately degrading carrier transport and photoresponse.

ACKNOWLEDGMENT

The authors gratefully acknowledge the Centre for Design and Fabrication of Electronic Devices (C4DFED), Advanced Materials Research Centre (AMRC), Indian Institute of Technology (IIT) Mandi, Mandi (Himachal Pradesh), India for providing state-of-the-art device fabrication and characterization facilities for this work.

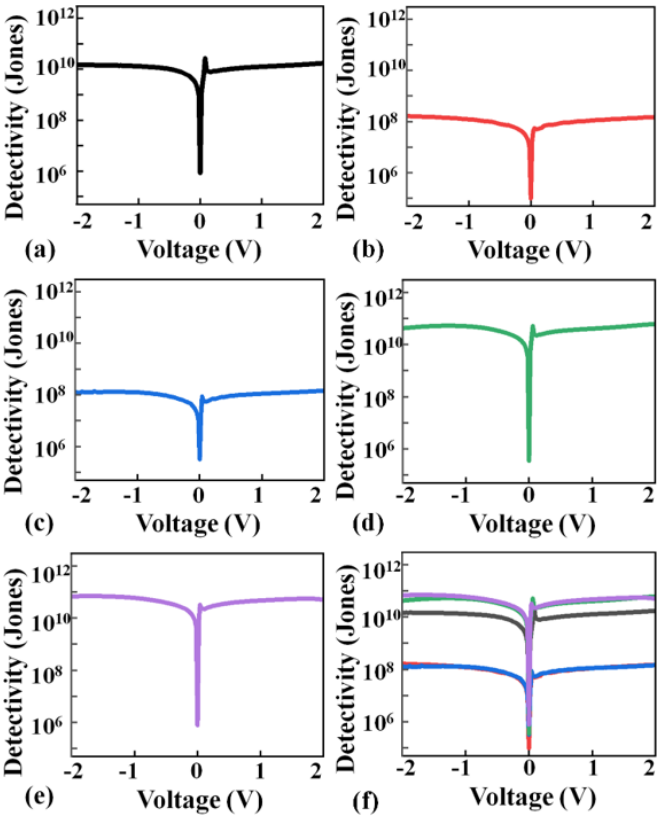


FIG. 11. Detectivity plot for different concentrations of Zn doping. (a) 0% Zn-doped, (b) 0.5% Zn-doped, (c) 1% Zn-doped, (d) 3% Zn-doped, and (e) 5% Zn-doped gallium oxide UV detector, and (f) comparative plots of all the doped samples.

DATA AVAILABILITY

There are no publicly available research data or software supporting this manuscript. Requests for further information or data should be sent to the authors.

[1] M. Razeghi and A. Rogalski, Semiconductor ultraviolet detectors, J. Appl. Phys. **79**, 7433 (1996).

[2] S. Nakagomi, Ultraviolet photodetector based on a beta-gallium oxide/nickel oxide/beta-gallium oxide heterojunction structure, Sensors **23**, 8332 (2023).

[3] S. H. Lee, S. B. Kim, Y. J. Moon, S. M. Kim, H. J. Jung, M. S. Seo, K. M. Lee, S. K. Kim, and S. W. Lee, High-responsivity deep-ultraviolet-selective photodetectors using ultrathin gallium oxide films, ACS Photon. **4**, 2937 (2017).

[4] P. Mukhopadhyay, I. Hatipoglu, Y. K. Frodason, J. B. Varley, M. S. Williams, D. A. Hunter, N. K. Gunasekar, P. R. Edwards, R. W. Martin, F. Wu, A. Mauze, J. S. Speck, and W. V. Schoenfeld, Role of defects in ultra-high gain in fast planar tin gallium oxide UV-C photodetector by MBE, Appl. Phys. Lett. **121**, 111105 (2022).

[5] P. Schlupp, D. Splith, H. von Wenckstern, and M. Grundmann, Electrical properties of vertical *p*-NiO/*n*-Ga_2O_3 and *p*-$ZnCo_2O_4$/*n*-Ga_2O_3 *pn*-heterodiodes, Phys. Status Solidi A **216**, 1800729 (2019).

[6] T. M. H. Nguyen, M. H. Tran, and C. W. Bark, Growth of low-defect Si-doped Ga_2O_3 film on fluorine-doped tin oxide substrate for self-powered and high-performance ultraviolet photodetector, ACS Appl. Electron. Mater. **5**, 6459 (2023).

[7] X. Lu, Y. Deng, Y. Pei, Z. Chen, and G. Wang, Recent advances in NiO/Ga_2O_3 heterojunctions for power electronics, J. Semicond. **44**, 061802 (2023).

[8] A. I. Titov, K. V. Karabeshkin, A. I. Struchkov, V. I. Nikolaev, A. Azarov, D. S. Gogova, and P. A. Karaseov, Comparative study of radiation tolerance of GaN and Ga_2O_3 polymorphs, Vacuum **200**, 111005 (2022).

[9] A. E. Romanov, S. I. Stepanov, V. I. Nikolaev, and V. E. Bougrov, Gallium oxide: Properties and applications—A review, Rev. Adv. Mater. Sci. **44**, 63 (2016).

[10] X. Chen, F. Ren, S. Gu, and J. Ye, Review of gallium-oxide-based solar-blind ultraviolet photodetectors, Photon. Res. **7**, 381 (2019).

[11] K. Arora, N. Goel, M. Kumar, and M. Kumar, Ultrahigh performance of self-powered β-Ga_2O_3 thin film solar-blind photodetector grown on cost-effective Si substrate using high-temperature seed layer, ACS Photon. **5**, 2391 (2018).

[12] T. K. O. Vu, D. U. Lee, and E. K. Kim, The enhancement mechanism of photo-response depending on oxygen pressure for Ga_2O_3 photo detectors, Nanotechnology **31**, 245201 (2020).

[13] K. H. Li, N. Alfaraj, C. H. Kang, L. Braic, M. N. Hedhili, Z. Guo, T. K. Ng, and B. S. Ooi, Deep-ultraviolet photodetection using single-crystalline β-Ga_2O_3/NiO heterojunctions, ACS Appl. Mater. Interfaces **11**, 35095 (2019).

[14] A. S. Pratiyush, S. Krishnamoorthy, S. V. Solanke, Z. Xia, R. Muralidharan, S. Rajan, and D. N. Nath, High responsivity in molecular beam epitaxy grown β-Ga_2O_3 metal semiconductor metal solar blind deep-UV photodetector, Appl. Phys. Lett. **110**, 221107 (2017).

[15] A. Mondal, S. Nandi, M. K. Yadav, A. Nandi, and A. Bag, Broad range (254–302 nm) and high performance Ga_2O_3:SnO_2 based deep UV photodetector, IEEE Trans. Nanotechnol. **21**, 320 (2022).

[16] P. Ravadgar, R.-H. Horng, S.-D. Yao, H.-Y. Lee, B.-R. Wu, S.-L. Ou, and L.-W. Tu, Effects of crystallinity and point defects on optoelectronic applications of β-Ga_2O_3 epilayers, Opt. Express **21**, 24599 (2013).

[17] Y. Jin, J. Wang, B. Sun, J. C. Blakesley, and N. C. Greenham, Solution-processed ultraviolet photodetectors based on colloidal ZnO nanoparticles, Nano Lett. **8**, 1649 (2008).

[18] H. Shen, Y. Yin, K. Tian, K. Baskaran, L. Duan, X. Zhao, and A. Tiwari, Growth and characterization of β-Ga_2O_3 thin films by sol-gel method for fast-response solar-blind ultraviolet photodetectors, J. Alloys Compd. **766**, 601 (2018).

[19] M. K. Vronskii, A. Y. Ivanov, L. A. Sokura, A. V. Kremleva, and D. A. Bauman, Structural properties of β-Ga_2O_3 thin films obtained on different substrates by sol-gel method, Rev. Adv. Mater. Technol. **5**, 26 (2023).

[20] S. Kumar and R. Singh, Nanofunctional gallium oxide (Ga_2O_3) nanowires/nanostructures and their applications in nanodevices, Phys. Status Solidi RRL **7**, 781 (2013).

[21] J. R. Vig, UV/ozone cleaning of surfaces, Proc. Electrochem. Soc. **90**, 105 (1990).

[22] Y. Zhu, X. Xiu, F. Cheng, Y. Li, Z. Xie, T. Tao, P. Chen, B. Liu, R. Zhang, and Y. D. Zheng, Growth and nitridation of β-Ga_2O_3 thin films by sol-gel spin-coating epitaxy with post-annealing process, J. Sol-Gel Sci. Technol. **100**, 183 (2021).

[23] Y. Yao, Y. Ishikawa, and Y. Sugawara, X-ray diffraction and Raman characterization of β-Ga_2O_3 single crystal grown by edge-defined film-fed growth method, J. Appl. Phys. **126**, 205106 (2019).

[24] M. Bartic, C.-I. Baban, H. Suzuki, M. Ogita, and M. Isai, β-gallium oxide as oxygen gas sensors at a high temperature, J. Am. Ceram. Soc. **90**, 2879 (2007).

[25] L. X. Qian, Z. H. Wu, Y. Y. Zhang, P. T. Lai, X. Z. Liu, and Y. R. Li, Ultrahigh-responsivity, rapid-recovery, solar-blind photodetector based on highly nonstoichiometric amorphous gallium oxide, ACS Photon. **4**, 2203 (2017).

[26] G. Wu, Y. Xu, Y. Weng, F. Wu, and D. Guo, Achieving programmable bipolar photocurrents via *p*–*n* junction design for PEPS-based optoelectronic applications, Appl. Phys. Lett. **128**, 113305 (2026).

[27] W. Yue, J. Yan, J. Wu, and L. Zhang, Structural and optical properties of Zn-doped β-Ga_2O_3 films, J. Semicond. **33**, 073003 (2012).

[28] H. Liu, C. Xu, X. Pan, and Z. Ye, The photoluminescence properties of β-Ga_2O_3 thin films, J. Electron. Mater. **49**, 4544 (2020).
[29] K. Wang, Z. Wu, H. Tong, Z. Zeng, J. Kim, W. Cai, J. Jin, and Z. Zang, Development and challenges of Ga_2O_3-based heterojunctions for deep-UV detectors, ACS Photon. **12**, 4851 (2025).
[30] G. Wu, X. Guo, F. Zhang, X. Zhong, J. Wang, and D. Guo, Radiation damage mechanisms in β-Ga_2O_3 MSM solar-blind photodetectors: Insights from proton, neutron, and γ-ray irradiation, IEEE Electron Device Lett. **46**, 2086 (2025).
[31] Y. Zhao and R. L. Frost, Raman spectroscopy and characterisation of α-gallium oxyhydroxide and β-gallium oxide nanorods, J. Raman Spectrosc. **39**, 1494 (2008).
[32] M. K. Yadav, A. Mondal, S. K. Sharma, and A. Bag, Unveiling thermal effects on Sn-doped β-Ga_2O_3 Schottky barrier diodes on sapphire for high-temperature power electronics, IEEE Trans. Electron Devices **71**, 1529 (2024).
[33] M. K. Yadav, A. Mondal, S. K. Sharma, and A. Bag, Probing interface trapping characteristics of Au/β -Ga_2O_3 Schottky barrier diode on Si (100), IEEE Trans. Device Mater. Reliab. **21**, 613 (2021).
[34] S. Sharma, R. Khosla, D. Deva, H. Shrimali, and S. K. Sharma, Fluorine-chlorine co-doped TiO_2/CSA doped polyaniline based high performance inorganic/organic hybrid heterostructure for UV photodetection applications, Sens. Actuators A Phys. **261**, 94 (2017).
[35] R. Khosla, E. G. Rolseth, P. Kumar, S. S. Vadakupudhupalayam, S. K. Sharma, and J. Schulze, Charge trapping analysis of metal/Al_2O_3/SiO_2/Si, gate stack for emerging embedded memories, IEEE Trans. Device Mater. Reliab. **17**, 80 (2017).
[36] J. Hu, B. Yu, and J. Zhou, New generation beta-gallium oxide nanomaterials: Growth and performances in electronic devices, Adv. Eng. Mater. **25**, 2300688 (2023).
[37] S. Averine, Y. C. Chan, and Y. L. Lam, Electrical properties of Schottky barrier in MSM-diode structures, in *2000 International Semiconducting and Insulating Materials Conference*, SIMC-XI (Cat. No. 00CH37046) (IEEE, Canberra, ACT, Australia, 2000), pp. 345–348.
[38] D. Guo, X. Qin, M. Lv, H. Shi, Y. Su, G. Yao, S. Wang, C. Li, P. Li, and W. Tang, Decrease of oxygen vacancy by Zn-doped for improving solar-blind photoelectric performance in β-Ga_2O_3 thin films, Electron. Mater. Lett. **13**, 483 (2017).
[39] F. Alema, B. Hertog, O. Ledyaev, D. Volovik, G. Thoma, R. Miller, A. Osinsky, P. Mukhopadhyay, S. Bakhshi, H. Ali, and W. V. Schoenfeld, Solar blind photodetector based on epitaxial zinc doped Ga_2O_3 thin film, Phys. Status Solidi A **214**, 1600688 (2017).
[40] J. Wang, X. Ji, Z. Yan, S. Qi, X. liu, A. Zhong, and P. Li, The role of oxygen vacancies in Ga_2O_3-based solar-blind photodetectors, J. Alloys Compd. **970**, 172448 (2024).
[41] M. Yu, C. Lv, J. Yu, Y. Shen, L. Yuan, J. Hu, S. Zhang, H. Cheng, Y. Zhang, and R. Jia, High-performance photodetector based on sol–gel epitaxially grown α/β Ga_2O_3 thin films, Mater. Today Commun. **25**, 101532 (2020).
[42] Y. Zhu, Y. Li, X. Xiu, X. Sun, Z. Xie, T. Tao, P. Chen, B. Liu, J. Ye, R. Zhang, and Y. Zheng, Preparation of β-Ga_2O_3 films on off-angled sapphire substrates and solar-blind ultraviolet photodetectors, J. Phys. D: Appl. Phys. **55**, 424001 (2022).
[43] H. Lu, X. Chen, S. Qiao, J. Chen, J. Mao, H. Zhu, P. Li, Y. Lu, and Y. He, High-performance self-driven ultraviolet photodetector based on sol–gel derived NiO/Sn:Ga_2O_3 p–n junction, ACS Appl. Electron. Mater. **8**, 3985 (2026).
[44] Y. Choi, S. S. Lee, W. J. Lee, and I. K. Park, Zn-doping induced phase control mechanism of Ga_2O_3 thin films by spray pyrolysis deposition for application of solar-blind ultraviolet photodetector, Mater. Today Chem. **33**, 101738 (2023).